Supplementary Material

Interface engineering of heterostructured NiSn@NiMn-LDH as a bifunctional electrocatalyst for oxygen evolution reaction and hydrogen evolution reaction

Wei Gao[a,b,*], Chao He[a], Yuzun Li[a], Yufeng Li[a,*], Weiwei Tang[a], Zhe Zhang[a], Houxiang Sun[a], Jitao Zhao[c]

[a] School of Biological and Chemistry Engineering, Panzhihua University, Panzhihua, 617000, China

[b] Sichuan Technology & Engineering Research Center for Vanadium Titanium Materials, Panzhihua, 617000, China

[c] School of Civil and Architecture Engineering, Panzhihua University, Panzhihua, 617000, China

***Corresponding Authors**

Wei Gao, E-mail:15046674011@163.com

Yufeng Li, E-mail: lyfpzh308@163.com

1. Experimental

1.1 Chemicals

$NiCl_2 \cdot 6H_2O$, $MnCl_2 \cdot 4H_2O$, $SnCl_2 \cdot 2H_2O$, ethyl alcohol, NaOH, KOH were bought from Shinopharm Chemical Reagent Co., Ltd. RuO_2, Nafion (5 wt%) were obtained by Aladdin Chemical Reagent Co., Ltd. $NaH_2PO_2 \cdot H_2O$ was bought from Xiya Chemical Technology (Shandong) Co., Ltd. Ti mesh was used as the supporting material.

1.2 Pretreatment of TM

TM was introduced into 2 mol L^{-1} HCl, ethanol, deionized water and ultrasonicated for 20 min with the aim of removing the oxide layer on the surface of TM. The cleaned TM was obtained after drying at 60 ^{o}C for 1 h in a vacuum oven.

1.3 Synthesis of RuO_2/TM

3.21 mg RuO_2 powder was dispersed in 50 μL of deionized water, 50 μL of ethanol, and 14 μL of 5 wt.% Nafion solution, and ultrasonically treated for a certain period of time to form a even suspension. Afterwards, 38 μL of the above-mentioned uniform suspension was coated on the surface of TM (1×1 cm^2). After drying at room temperature for 24 h, RuO_2/TM electrode was obtained. The average mass load of RuO_2 on TM surface was approximately 1.07 mg cm^{-2}.

1.4 Materials characterization

Rigaku Ultima IV X-ray diffraction (XRD) with Cu Kα radiation (λ = 1.540538 Å) was used to investigate the crystalline structure of samples. Thermo Scientific K-Alpha X-ray photoelectron spectroscopy (XPS) was applied to explain the composition and valence state of samples. Thermo Scientific Apreo 2C field emission scanning electron microscope (SEM) was used to observe the microstructure and morphology of samples, and the elemental distribution state of samples was investigated by OXFORD ULTIM Max 65 energy-dispersive X-ray spectroscopy, which was attached with SEM. The mass load of as-constructed electrocatalysts on the surface of TM was tested by PE Avio 200 ICP-OES.

1.5 Electrochemical measurements

The electrochemical activity was evaluated by CS315M electrochemical station (Corrtest Instrument Corp., Ltd, Wuhan). OER and HER were measured through three electrode system with Pt mesh as counter electrode, mercury oxide electrode (Hg/HgO) as reference electrode, the constructed electrode as working electrode. What's more, electrolytic solution was 1 mol L^{-1} KOH, and the pH=13.88.

For a better comparison, the Hg/HgO potential was converted to a reversible hydrogen electrode (RHE) based on equation S1

$$E_{\mathrm{RHE}}=E_{\mathrm{Hg/HgO}}+0.059\times\mathrm{pH}+0.098=E_{\mathrm{Hg/HgO}}+0.0917 \tag{S1}$$

The potentials of linear sweep voltammetry (LSV) curves of OER and HER were corrected by iR compensation, which were calculated by Eq. S2 and Eq. S3:

$$E_{compensated}(OER)=E_{measured}(OER)-iR \tag{S2}$$

$$E_{compensated}(HER)=E_{measured}(HER)-iR \tag{S3}$$

The overpotential (η) was used to estimate OER and HER activity. η was calculated by Eq. S4 and Eq. S5,

$$\eta(V,OER)=E_{RHE}(OER)-1.23 \tag{S4}$$

$$\eta(V,HER)=0-E_{RHE}(HER) \tag{S5}$$

Tafel slope was applied to estimate catalytic and kinetics of as-constructed electrode toward OER and HER, which was acquired through fitting the linear region of LSV curve. Tafel slope was obtained by Eq. S6 [1]:

$$\eta=a+b\log J \tag{S6}$$

Where J is the current density.

The effective electrochemical active surface area (ECSA) of the constructed electrode was acquired through CV curves at non-faradaic domain from 0.02 V to 0.12 V at the scan rates of 50, 100, 150 200 and 250 mV s^{-1}. The geometric double layer capacitance (C_{dl}) was the slope value by plotting the difference of current density (ΔJ) between the anodic and cathodic sweeps ($J_{\mathrm{anodic}}-J_{\mathrm{cathodic}}$)/2 against the scan rate. In particular, ECSA value was estimated by C_{dl} basing on Eq. S7,

$$\mathrm{ECSA} = \frac{C_{dl}}{C_s} \tag{S7}$$

Where C_s is the specific capacitance, and C_s is estimated to the value of 0.04 mF cm^{-2} [2, 3].

The roughness factor (RF) was calculated by Eq. S8:

$$\mathrm{RF} = \frac{ECSA}{GSA} \tag{S8}$$

where GSA is the geometric surface area of the electrode, the value is 1.0 cm^{-2} in this research.

J_{ECSA} represented the normalization of J with ECSA, which was estimated by Eq. S9,

$$J_{ECSA} = \frac{J}{ECSA} \tag{S9}$$

where J is the current density.

Electrocatalytic stability of OER and HER was measured through successive CV curves, multipotential test, multicurrent test and chronoamperometry test.

(1) OER

CV curves were carried out in the potential of 0 ~ 1.3 V vs. $E_{\mathrm{Hg/HgO}}$ at 40 mV s^{-1} for 1000 cycles. Electrochemical impedance spectroscopy (EIS) was performed in the range of 0.01~10^5 Hz at 5 mV with the potential of 1.617 V vs. RHE. Multipotential experiment was carried out from 1.617 V vs. RHE to 2.117 V vs. RHE with a step of 0.1 V, then from 2.117 V vs. RHE to 1.617 V vs. RHE with a step of -0.1 V. Multicurrent experiment was performed with the range of 50 ~ 300 mA cm^{-2} at a step of 50 mA cm^{-2}, subsequently, from 300 mA cm^{-2} to 50 mA cm^{-2} at a step of -50 mA cm^{-2}. The stability experiment was carried out through the chronoamperometry (J–t) at 30 mA cm^{-2} for 50 h.

(2) HER

CV curves were carried out in the range of -1.8 ~ -0.8 V vs. $E_{\mathrm{Hg/HgO}}$ at 40 mV s^{-1} for 1000 cycles. EIS was performed in the range of 0.01~10^5 Hz at 5 mV with the potential of -0.283 V. Multipotential experiment was carried out from -0.783 V vs. RHE to -0.283 V vs. RHE with a step of 0.1 V, then from -0.283 V vs. RHE to -0.783

V vs. RHE with a step of -0.1 V. Multicurrent experiment was performed from -300 mA cm^{-2} to -50 mA cm^{-2} at a step of 50 mA cm^{-2}, then from -50 mA cm^{-2} to -300 mA cm^{-2} at a step of -50 mA cm^{-2}. The stability experiment was carried out through J–t at -50 mA cm^{-2} for 50 h.

2. Supplementary Figures

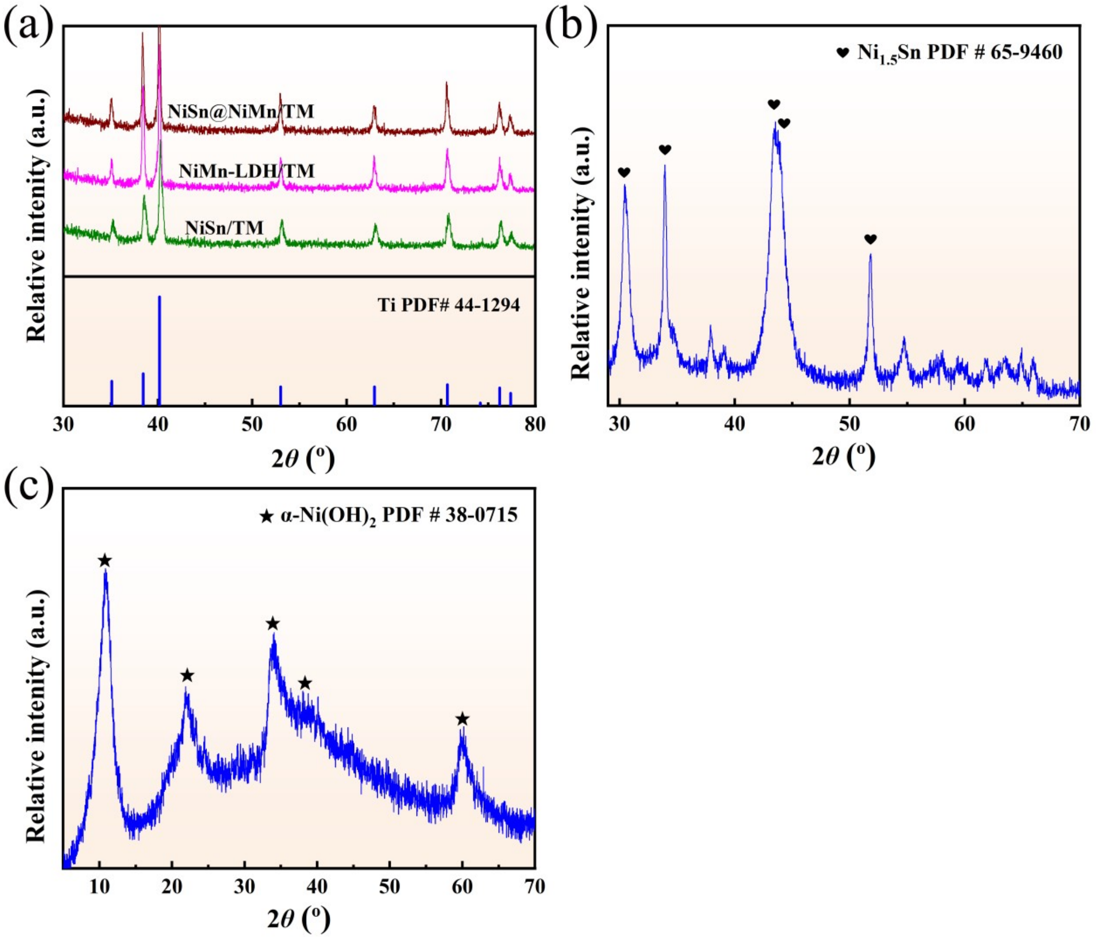

Fig. S1 XRD patterns of as-prepared samples, (a) NiSn/TM, NiMn-LDH/TM, NiSn@NiMn-LDH/TM, (b) NiSn powder, (c) NiMn-LDH powder.

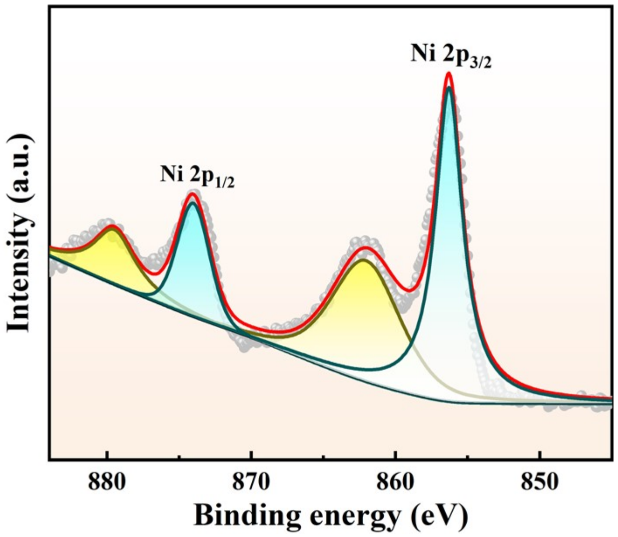

Fig. S2 Ni 2p spectrum of NiSn@NiMn-LDH/TM.

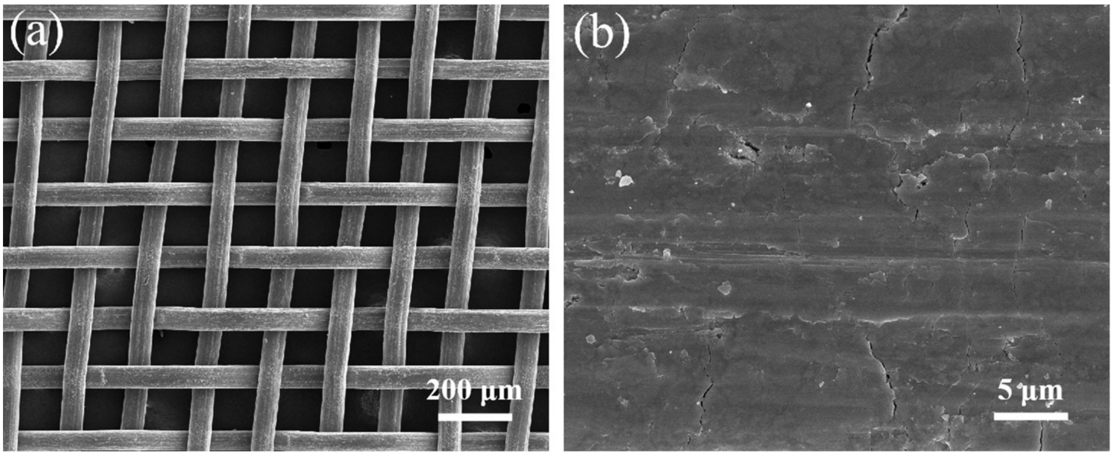

Fig. S3 SEM images of TM at different magnification (a) low-magnification, (b) high-magnification.

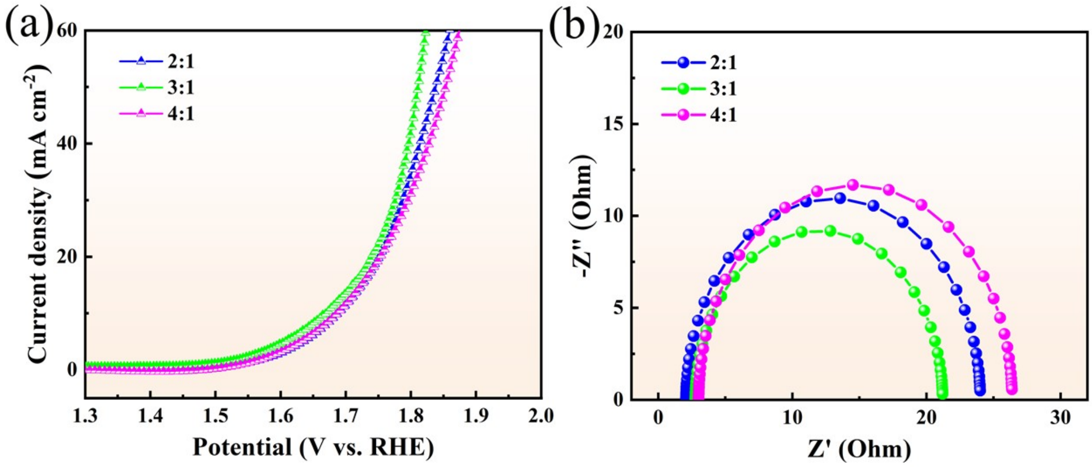

Fig. S4 OER performance of NiSn/TM electrode with the different molar ratio of Ni to Sn, (a) LSV curves, (b) EIS Nyquist plots.

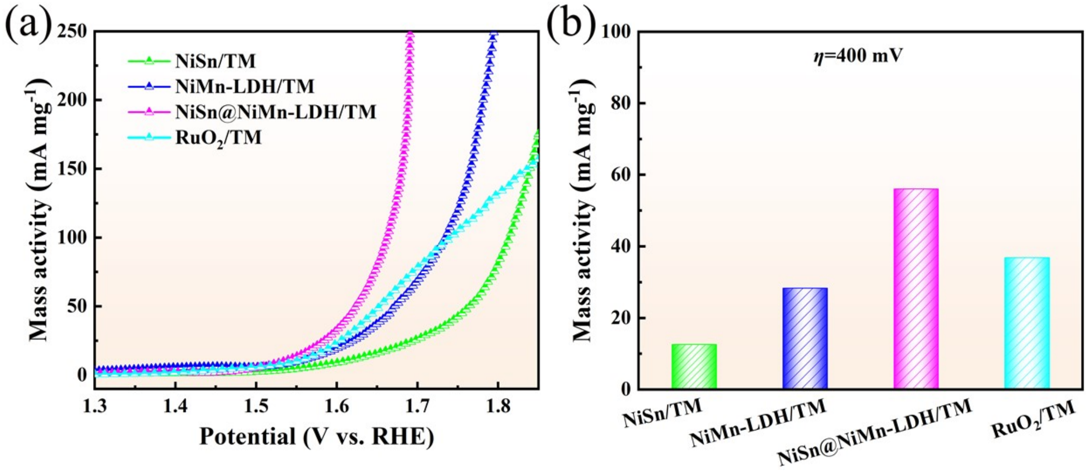

Fig. S5 (a) Mass activity curves of the as-fabricated electrocatalysts, (b) Mass activity values at the overpotential of 400 mV for OER.

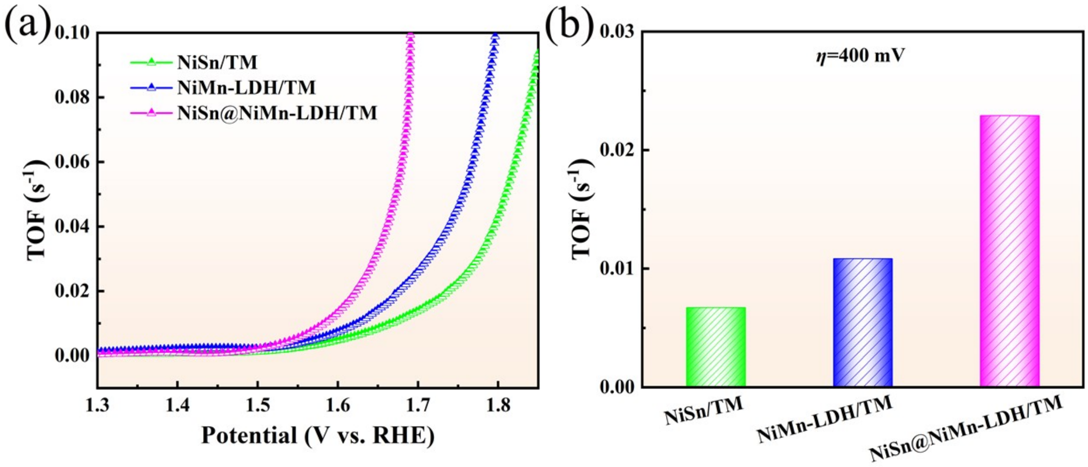

Fig. S6 (a) TOF curves of the as-fabricated electrocatalysts, (b) TOF values at the overpotential of 400 mV for OER.

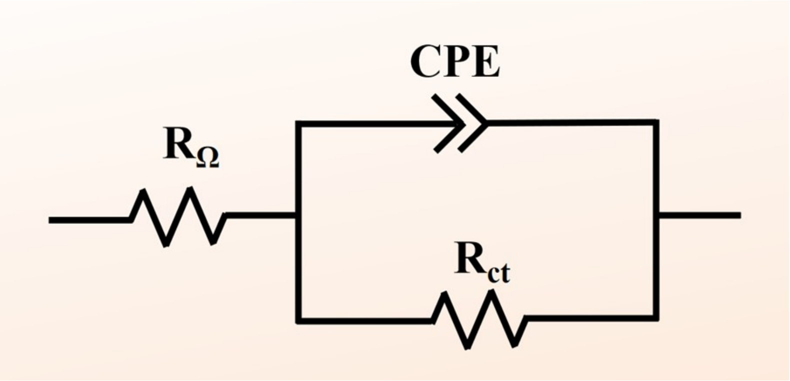

Fig. S7 Equivalent circuit model (Randle's circuit) for EIS plot fitting.

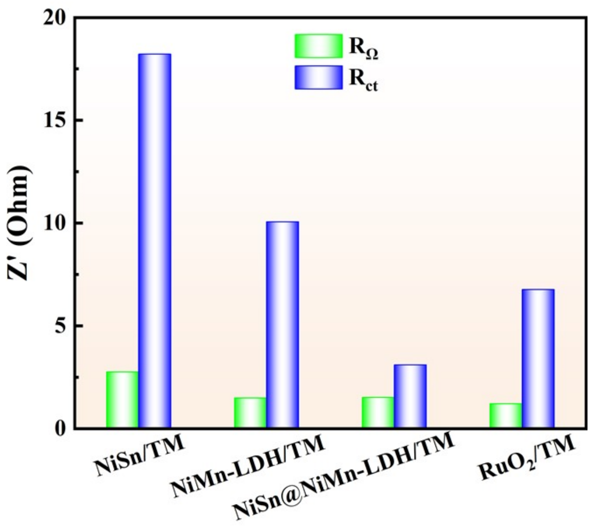

Fig. S8 EIS parameter at 1.617 V vs. RHE for OER.

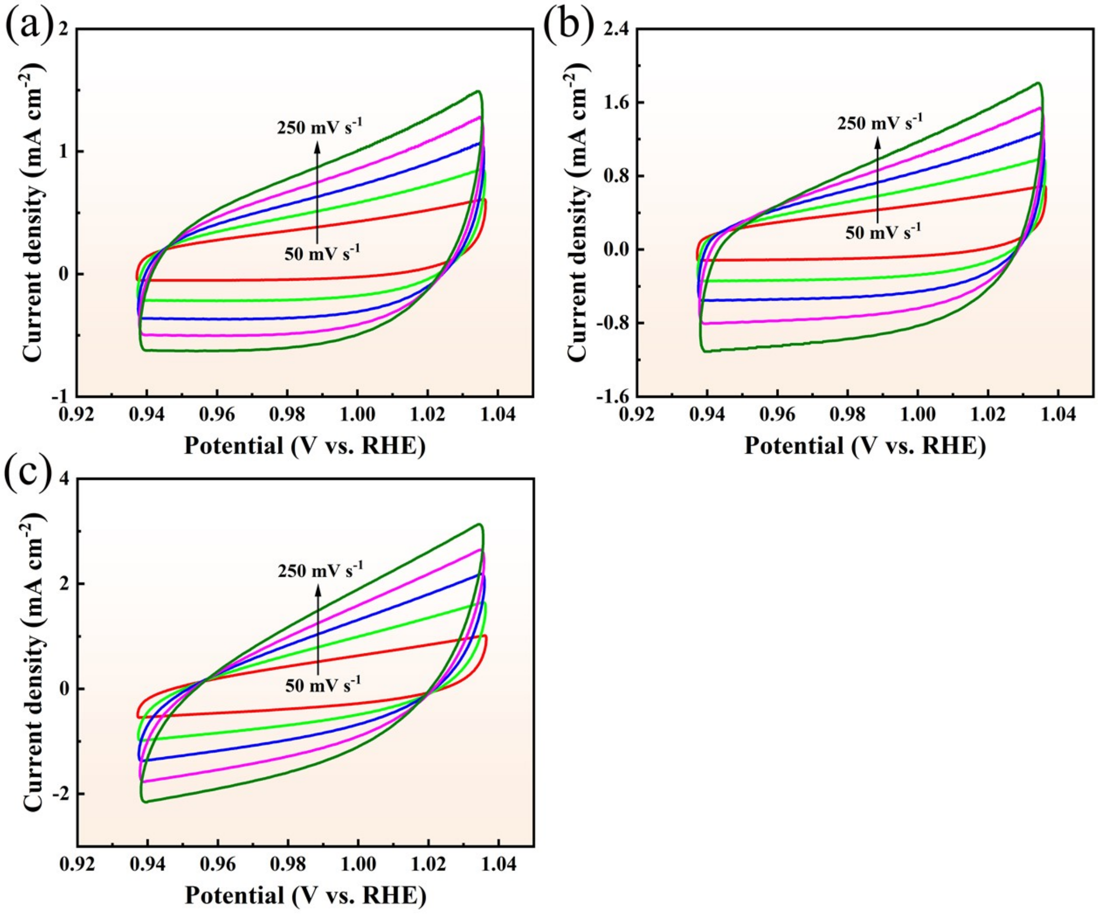

Fig. S9 CV curves of (a) NiSn/TM, (b) NiMn-LDH/TM, (c) NiSn@NiMn-LDH/TM at the scanning rates of 50, 100, 150, 200, 250 mV s^{-1} in 1 M KOH with the potential of 0.937~1.037 V vs. RHE (OER).

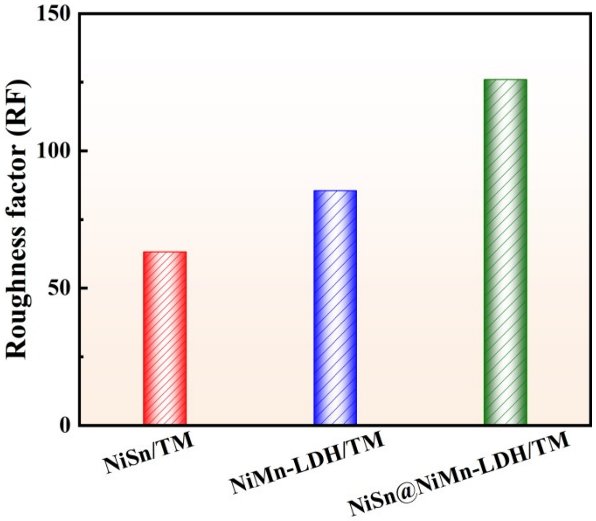

Fig. S10 Roughness factor of the as-constructed electrodes for OER.

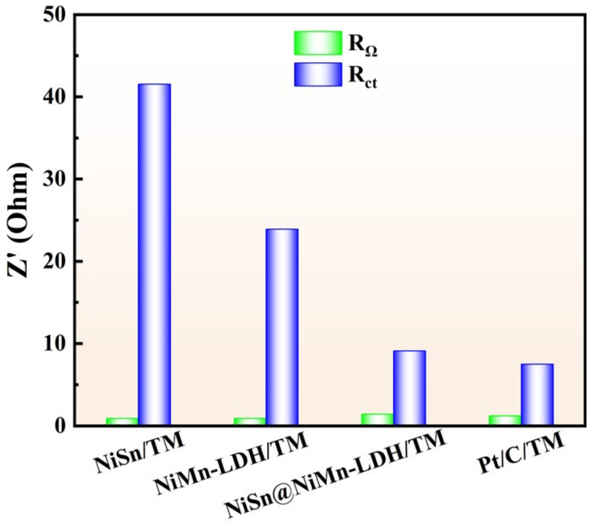

Fig. S11 EIS parameter at -0.283 V vs. RHE for HER.

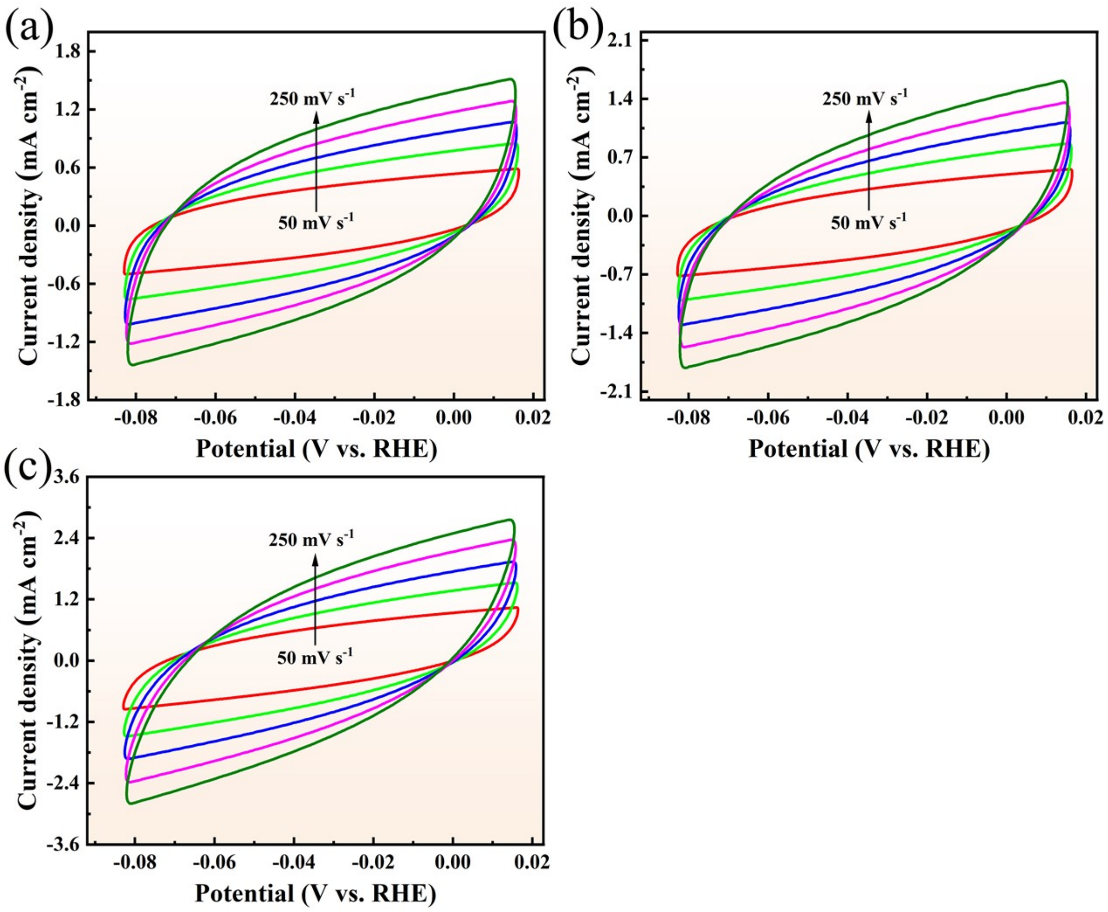

Fig. S12 CV curves of (a) NiSn/TM, (b) NiMn-LDH/TM, (c) NiSn@NiMn-LDH/TM at the scanning rates of 50, 100, 150, 200, 250 mV s^{-1} in 1 M KOH with the potential of -0.083~-0.017 V vs. RHE (HER).

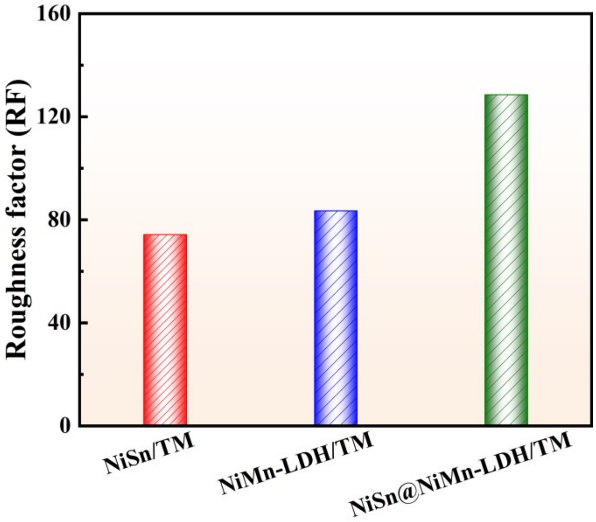

Fig. S13 Roughness factor of the as-constructed electrodes for HER.

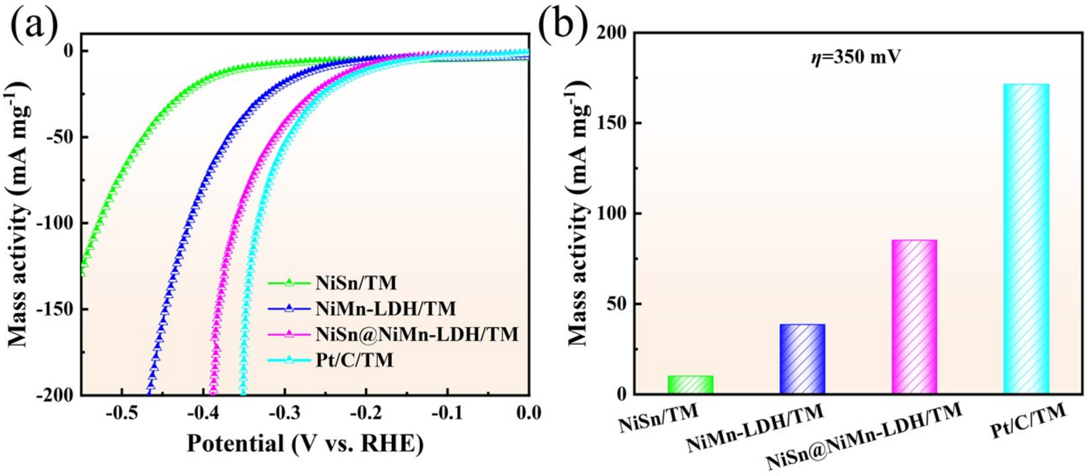

Fig. S14 (a) Mass activity curves of the as-fabricated electrocatalysts, (b) Mass activity values at the overpotential of 350 mV for HER.

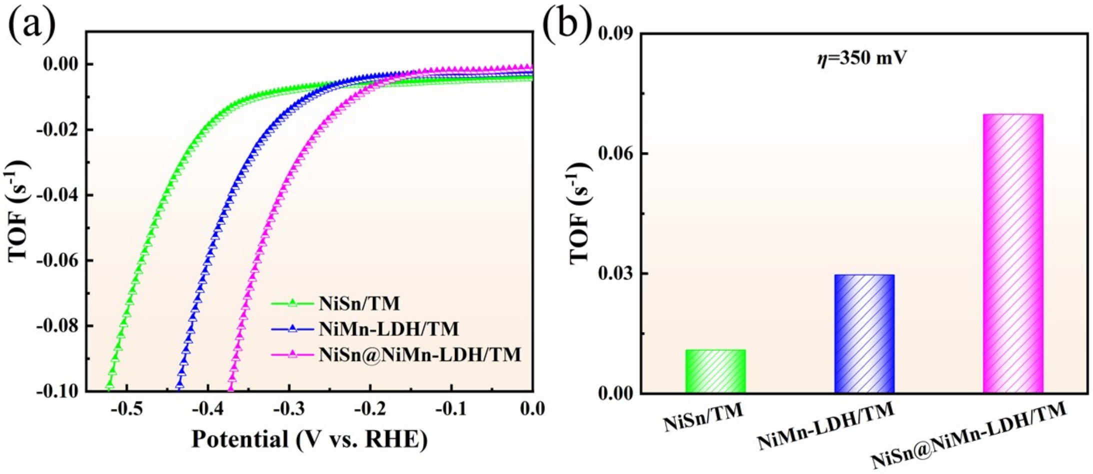

Fig. S15 (a) TOF curves of the as-fabricated electrocatalysts, (b) TOF values at the overpotential of 350 mV for HER.

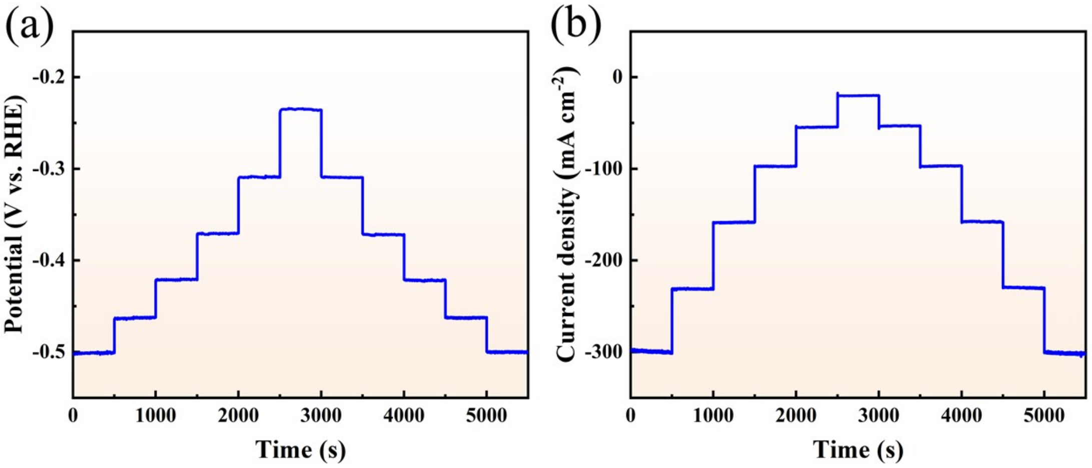

Fig. S16 The multicurrent and multipotential curves of NiSn@NiMn-LDH/TM for HER.

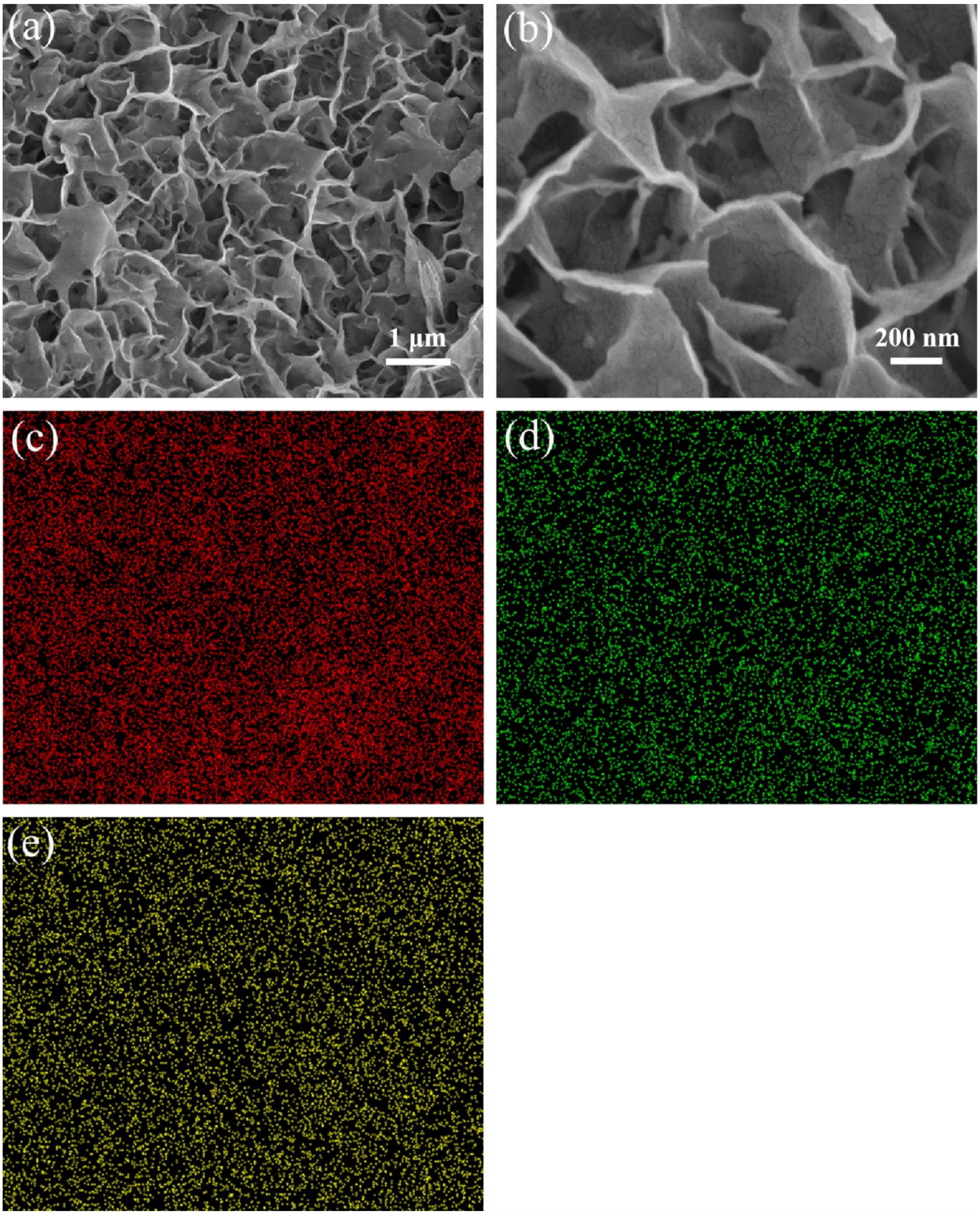

Fig. S17 SEM images (a, b) and EDS mapping images of (c) Ni, (d) Sn, (e) Mn for NiSn@NiMn-LDH/TM after stability test for OER.

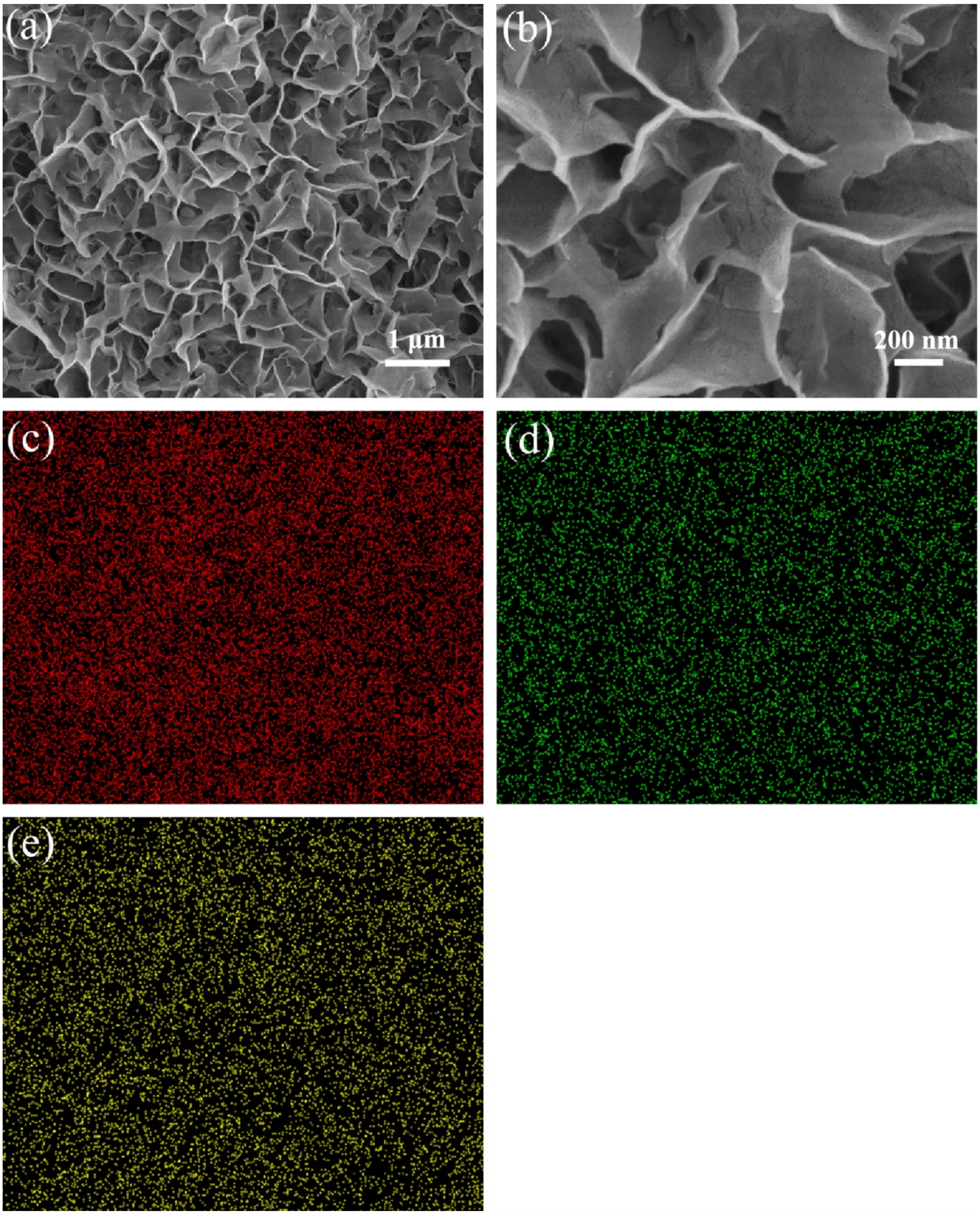

Fig. S18 SEM images (a, b) and EDS mapping images of (c) Ni, (d) Sn, and (e) Mn for NiSn@NiMn-LDH/TM after stability test for HER.

3. Supplementary Tables

Table S1 Comparison of the OER activity of NiSn@NiMn/TM with other reported non-noble metal-based electrocatalysts in 1.0 M KOH.

Electrocatalysts	**Substrate**	**Current density (mA/cm^2)**	**Overpotential (mV)**	**Reference**
NiSn@NiMn-LDH	TM	10	300.2	This work
		50	390.6	
$NiCo_2O_4@MoS_2$	TM	10	313	[4]
NiCoMn	TM	10	334.69	[5]
Co_3O_4@Ti-15	TM	50	416	[6]
NiMo	TM	10	310	[7]
W_2N/WC	Carbon clothes	10	320	[8]
Co_3S_4	Glassy carbon	10	350	[9]
CoOOH nanosheet	Carbon-coated chip	10	426	[10]
Co_2FeO_4	Glassy carbon	10	359	[11]
Fe-CoP nanoFC	NF	10	347	[12]
$Co_{2.25}Fe_{0.75}O_4$	Glassy carbon	10	350	[13]
Ar-U-CoFe PBA	NF	10	305	[14]
Yolk-shell Mn-CoP	/	10	330	[15]

Table S2 The summarized double layer capacitance (C_{dl}) and electrochemical surface area (ECSA) of the as-fabricated electrocatalysts for OER.

Electrocatalysts	**C_{dl} (mF cm^{-2})**	**ECSA (cm^2)**
NiSn/TM	2.53	63.25
NiMn-LDH/TM	3.42	85.50
NiSn@NiMn-LDH/TM	5.04	126.00

Table S3 Comparison of the HER activity of NiSn@NiMn/TM with other reported non-noble metal-based electrocatalysts in 1.0 M KOH.

Electrocatalysts	**Substrate**	**Current density (mA/cm^2)**	**Overpotential (mV)**	**Reference**
NiSn@NiMn-LDH	TM	10	202.6	This work
Ni/TM-360 s	TM	10	205	[16]
$MnNiCoFe-P_2$	TM	10	300	[5]
Mo doped CoS_x	TM	10	230	[17]
Au(NiMo)/Ti-3	TM	10	252	[18]
$Ni-NiFe_2O_4$@C	Carbon cloth	10	217	[19]
Co_3O_4/Ppy/MWCNT	Glassy carbon	10	290	[20]
Co SAs-Co NPs/NCFs	Glassy carbon	10	205	[21]
$Ni-CoSe_2$/BCT-900	Glassy carbon	10	250	[22]
$Ni_{0.09}Co_{2.91}O_4/Ti_3C_2T_x$-HT	Glassy carbon	10	210	[23]
$Mn-NiCo(OH)_2$/NF	NF	10	246	[24]
CoFe@NiFe/NF	NF	10	240	[25]
$NiMn_2O_4$/Ni-foam-175	NF	10	248	[26]

Table S4 The summarized double layer capacitance (C_{dl}) and electrochemical surface area (ECSA) of the as-fabricated electrocatalysts for HER.

Electrocatalysts	**C_{dl} (mF cm^{-2})**	**ECSA (cm^{2})**
NiSn/TM	2.97	74.25
NiMn-LDH/TM	3.34	83.50
NiSn@NiMn-LDH/TM	5.14	128.50

4. References

[1] M. Tahir, L. Pan, F. Idrees, X. Zhang, L. Wang, J. J. Zou, Z. L.Wang, Electrocatalytic oxygen evolution reaction for energy conversion and storage: a comprehensive review. Nano Energy 2017, 37: 136-157. https://doi.org/10.1016/j.nanoen.2017.05.022.

[2] L. Zhou, C. Yang, W. Zhu, R. Li, X. Pang, Y. Zhen, C. Wang, L. Gao, F. Fu, Z. Gao, Y. Liang, Boosting alkaline hydrogen evolution reaction via an unexpected dynamic evolution of molybdenum and selenium on $MoSe_2$ electrode. Adv Energy Mater 2022, 12: 2202367. https://doi.org/10.1002/aenm.202202367.

[3] S. Niu, W. J. Jiang, Z. Wei, T. Tang, J. Ma, J. S. Hu, L. J. Wan, Se-doping activates FeOOH for cost-effective and efficient electrochemical water oxidation. J. Am. Chem. Soc. 2019, 141: 7005-13. https://doi.org/10.1021/jacs.9b01214.

[4] W. Bao, Y. Li, J. Zhang, T. Ai, C. Yang, L. Feng, Interface engineering of the $NiCo_2O_4$@MoS_2/TM heterostructure to realize the efficient alkaline oxygen evolution reaction. Int. J. Hydrogen Energy 2023, 48: 12176-12184. https://doi.org/10.1016/j.ijhydene.2022.12.184.

[5] M. M. Hasan, A. K. Gomaa, G. E. Khedr, K. E. Salem, B. S. Shaheen, N. K. Allam, Highly durable compositionally variant bifunctional tetrametallic Ni-Co-Mn-Fe phosphide electrocatalysts synthesized by a facile electrodeposition method for high-performance overall water splitting. Energy Fuels 2022, 36: 14371-14381. https://doi.org/10.1021/acs.energyfuels.2c03266.

[6] Z. Tao, L. Jiang, X. Jia, H. Xiao, Y. Liang, B. Yang, P. Guo, L. Zhang, H. Yang, In situ growth of Co_3O_4 nanoneedles on titanium mesh for electrocatalytic oxygen evolution. J Mater Sci: Mater Electron 2021, 32: 23275-23284. https://doi.org/10.1007/s10854-021-06812-7.

[7] J. Tian, N. Cheng, Q. Liu, X. Sun, Y. He, A. M. Asiri, Self-supported NiMo hollow nanorod array: an efficient 3D bifunctional catalytic electrode for overall water splitting. J. Mater. Chem. A 2015, 3: 20056. https://doi.org/10.1039/C5TA04723D.

[8] J. Diao, Y. Qiu, S. Liu, W. Wang, K. Chen, H. Li, W. Yuan, Y. Qu, X. Guo, Interfacial engineering of W_2N/WC heterostructures derived from solid-state synthesis: A highly efficient trifunctional electrocatalyst for ORR, OER, and HER. Adv. Mater. 2019, 1905679. https://doi.org/10.1002/adma.201905679.

[9] R. Zhang, L. Pan, B. Guo, Z. F. Huang, Z. Chen, L. Wang, X. Zhang, Z. Guo, W. Xu, K.P. Loh, Tracking the role of defect types in Co_3O_4 structural evolution and active motifs during oxygen evolution reaction. J. Am. Chem. Soc. 2023, 145: 2271-2281. https://doi.org/10.1021/jacs.2c10515.

[10] S. Wang, Q. Jiang, S. Ju, C. S. Hsu, H. M. Chen, D. Zhang, F. Song, Identifying the geometric catalytic active sites of crystalline cobalt oxyhydroxides for oxygen evolution reaction. Nat. Commun. 2022, 13: 6650. https://doi.org/10.1038/s41467-022-34380-9.

[11] W. Xiang, N. Yang, X. Li, J. Linnemann, U. Hagemann, O. Ruediger, M. Heidelmann, T. Falk, M. Aramini, S. Debeer, 3D atomic-scale imaging of mixed Co-Fe spinel oxide nanoparticles during oxygen evolution reaction. Nat. Commun. 2022, 13: 179. https://doi.org/10.1038/s41467-021-27788-2.

[12] Y. Yuan, Y. Yang, H. Xie, X. Zhong, R. Wang, Z. Xu, Trace Fe doping improved the OER and HER catalytic performance of CoP hollow nanoflower clusters. Int. J. Hydrogen Energy 2024, 90: 1401-1410. https://doi.org/10.1016/j.ijhydene.2024.10.122.

[13] S. Saddeler, G. Bendt, S. Salamon, F. T. Haase, J. Landers, J. Timoshenko, C. Rettenmaier, H. S. Jeon, A. Bergmann, H. Wende, B. Roldan Cuenya, S. Schulz, Influence of the cobalt content in cobalt iron oxides on the electrocatalytic OER activity. J. Mater. Chem. A 2021, 9: 25381-25390. https://doi.org/10.1016/10.1039/d1ta06568h.

[14] F. Diao, M. R. Kraglund, H. Cao, X. Yan, P. Liu, C. Engelbrekt, X. Xiao, Moderate heat treatment of CoFe Prussian blue analogues for enhanced oxygen evolution reaction performance. J. Energy Chem. 2023, 78: 476-486. https://doi.org/10.1016/j.jechem.2022.11.050.

[15] Y. V. Kaneti, Y. Guo, N. L. W. Septiani, M. Iqbal, X. Jiang, T. Takei, B. Yuliarto, Z. A. Alothman, D. Golberg, Y. Yamauchi, Self-templated fabrication of hierarchical hollow manganese-cobalt phosphide yolk-shell spheres for enhanced oxygen evolution reaction. Chem. Eng. J. 2021, 405: 126580. https://doi.org/10.1016/j.cej.2020.126580.

[16] J. Wang, Y. Wang, T. Xie, Q. Deng, Facile and fast synthesis of Ni composite coating on Ti mesh by electrodeposition method for high-performance hydrogen production. Mater. Lett. 2019, 245: 138-141. https://doi.org/10.1016/j.matlet.2019.02.119.

[17] J. Wang, Y. Wang, Z. Yao, T. Xie, S. Liu, Z. Jiang, Mo doped amorphous CoS_x porous leaf-like nanostructure on Ti mesh as electrocatalyst for alkaline hydrogen production. J. Electrochem. Soc. 2020, 167: 114510. https://orcid.org/0000-0002-1044-1948.

[18] S. Barua, A. Balciunaite, J. Vaiciuniene, L. Tamašauskaite-Tamašiunaite, E. Norkus, Three-dimensional Au(NiMo)/Ti catalysts for efficient hydrogen evolution reaction. Materials 2022, 15: 7901. https://doi.org/10.3390/ma15227901.

[19] J. F. Zhang, Y. Jiang, Y. Wang, C. P. Yu, J. W. Cui, J. J. Wu, X. Shu, Y. Q. Qin, J. Sun, J. Yan, H. M. Zheng, Y. Zhang, Y. C. Wu, Ultrathin carbon coated mesoporous Ni-$NiFe_2O_4$ nanosheet arrays for efficient overall water splitting. Electrochim. Acta 2019, 321: 134652. https://doi.org/10.1016/j.electacta.2019.134652.

[20] S. S. Jayaseelan, N. Bhuvanendran, Q. Xu, H. N. Su, Co_3O_4 nanoparticles decorated Polypyrrole/carbon nanocomposite as efficient bi-functional electrocatalyst for electrochemical water splitting. Int. J. Hydrog. Energy 2020, 45: 4587-4595. https://doi.org/10.1016/j.ijhydene.2019.12.085.

[21] M. Wang, M. Li, Y. Zhao, N. Shi, H. Zhang, Y. Zhao, Y. Zhang, H. Zhang, W. Wang, K. Sun, Y. Pan, S. Liu, H. Zhu, W. Guo, Y. Li, Y. Liu, C. Liu, Construction of N-doped carbon frames anchored with Co single atoms and Co nanoparticles as robust electrocatalyst for hydrogen evolution in the entire pH range. J. Energy Chem. 2022, 67: 147-156. https://doi.org/10.1016/j.jechem.2021.09.037.

[22] G. Yang, Y. Zhang, J. Liu, M. Wang, C. Gu, J. Li, In-situ growth of Ni-$CoSe_2$ on biomass-derived carbon tubes as an efficient electrocatalyst for overall water splitting. Int. J. Hydrogen Energy 2022, 47: 38920-38929. https://doi.org/10.1016/j.ijhydene.2022.09.067.

[23] P. Xu, H. Wang, J. Liu, X. Feng, W. Ji, C.-T. Au, High-performance $Ni_xCo_{3-x}O_4/Ti_3C_2T_x$-HT interfacial nanohybrid for electrochemical overall water splitting. ACS Appl. Mater. Interfaces 2021, 13: 34308-34319. https://doi.org/10.1021/acsami.1c08032.

[24] W. Xia, X. Luan, W. Zhang, D. Wu, Sulfuration of hierarchical Mn-doped NiCo LDH heterostructures as efficient electrocatalyst for overall water splitting. Int. J. Hydrogen Energy 2023, 48: 27631-27641. https://doi.org/10.1016/j.ijhydene.2023.03.447.

[25] R. Yang, Y. Zhou, Y. Xing, D. Li, D. Jiang, M. Chen, W. Shi, S. Yuan, Synergistic coupling of CoFe-LDH arrays with NiFe-LDH nanosheet for highly efficient overall water splitting in alkaline media. Appl. Catal. B 2019, 253: 131-139. https://doi.org/10.1016/j.apcatb.2019.04.054.

[26] P.C. Nagajyothi, K. Pavani, R. Ramaraghavulu, Jaesool Shim, Microwave synthesis of $NiMn_2O_4$/Ni-foam: Efficient bifunctional electrocatalysts for overall water splitting. Int. J. Hydrogen Energy 2024, 54: 691-699. https://doi.org/10.1016/j.ijhydene.2023.09.046.